A Three-Level Hierarchical Power Smoothing Control Strategy for Pavement Photovoltaics Under Vehicle Shadow Disturbance

Mingxuan Mao, Yuhao Tang, Fuping Ma, Haojin Sun, Guoxiang Hua, and Peng Li

***Abstract*—In this article, a three-level hierarchical power smoothing control strategy is proposed for optimizing the pavement photovoltaic (PV) power fluctuation under vehicle shadowing disturbance. By applying the virtual impedance current-voltage droop control strategy to the inverter control link and impedance shaping the inverter branch and hybrid energy storage branch, a three-level crossover mechanism is constructed to achieve automatic crossover absorption of pavement PV power fluctuations and smooth control. Finally, the effectiveness of the proposed strategy is verified through simulation and experiment, and the influence of virtual impedance parameters on the system crossover mechanism is analyzed. The experimental results show that the proposed control strategy reduces the total harmonic distortion of the system output current from 17.09% to 8.23%, which greatly improves the power quality of the output power. The feasibility of the control strategy is verified in the scenario of indoor pavement PV system.**

***Index Terms*—Hybrid energy storage, pavement photovoltaics (PPVs), power smoothing control, virtual impedance.**

I. Introduction

PAVEMENT photovoltaic (PPV) power generation is an engineering practice application for smart roads [1], although it can make efficient use of land resources and achieve better environmental and economic benefits, it also brings new challenges [2]. In road traffic, some problems, such as volatility and uncertainty of photovoltaic (PV) power generation are amplified. Unlike the traditional PV multipeak problem caused by cloud shading, vehicle shadows with strong stochastic, fast-varying characteristics make PPV arrays not only have multipeak characteristics but also their *P-V* characteristics change at a faster rate, increasing the difficulty of executing maximum power tracking. As a result, PV power fluctuation characteristics become more complex, and the smoothing control of PV power becomes more challenging.

An energy storage system (ESS) is required to ensure stable PV power generation when connected to a microgrid. The system can smooth PV fluctuations, improve power quality, enhance system stability, regulate direct current (dc) bus voltage, assist frequency control, etc., thus effectively integrating PV power generation with the grid [3].

Because of their capacity to balance steady-state and dynamic responsiveness, battery-supercapacitor hybrid energy storage systems (HESSs) [4], [5] have drawn much interest and applications. According to the different advantages of batteries and supercapacitors, the types of power demand distributed in HESSs also have different focuses, and it remains a significant issue to determine how to achieve effective fluctuating power distribution.

In recent years, researchers have proposed various control strategies to achieve power distribution between hybrid energy storage. Depending on how the system is organized, these control strategies fall into two primary categories: centralized control and distributed control.

A. Centralized Power Smoothing Control Strategies

In the centralized control strategy, PV power is sampled by a central controller, which then uses a variety of signal processing techniques to extract the low-frequency and high-frequency components of the fluctuating power. Power commands are then sent to the hybrid energy storage through communication technology.

The centralized control strategy is further separated into filter-based control algorithms and optimization-based control algorithms [6]. The filter-based approach divides the system's power fluctuation response demand into high-frequency and low-frequency components, which are then responded to by the supercapacitor and battery, respectively. The most commonly used filtering techniques include high/low-pass filters (HPF/LPF) [7], wavelet transforms (WT) [8], empirical modal decomposition (EMD) [9], and sliding averaging (SA) [10], among others.

Received 31 March 2025; revised 4 July 2025 and 17 August 2025; accepted 21 August 2025. Date of publication 26 August 2025; date of current version 22 October 2025. This work was supported in part by the National Natural Science Foundation of China under Grant 52107177 and Grant 62073272, in part by the Wuxi University Research Start-up Fund for Introduced Talents under Grant 2024r025, and in part by the Jiangsu Shengneng Technology (Horizontal Project) under Grant 2024h049. Recommended for publication by Associate Editor C. Rojas. *(Corresponding author: Peng Li.)*

Mingxuan Mao, Haojin Sun, and Guoxiang Hua are with the School of Automation, Wuxi University, Wuxi 214105, China (e-mail: mx_m@cwxu.edu.cn; 22372318@stu.cwxu.edu.cn; hgx@cwxu.edu.cn).

Yuhao Tang and Peng Li are with the School of Automation, Wuxi University, Wuxi 214105, China, and also with the School of Automation, Nanjing University of Information Science and Technology, Nanjing 210044, China (e-mail: yuhaotang@nuist.edu.cn; 002036@nuist.edu.cn).

Fuping Ma is with Chengdu Power Supply Company, State Grid Sichuan Electric Power Company, Chengdu 610041, China (e-mail: 1740319184@qq.com).

Color versions of one or more figures in this article are available at https://doi.org/10.1109/TPEL.2025.3603016.

Digital Object Identifier 10.1109/TPEL.2025.3603016

The optimization-based control algorithms use control methods such as model predictive control (MPC) [11], [12], artificial neural networks (ANN) [13], and fuzzy logic control (FLC) [14], [15] to achieve power distribution inside the HESS.

Since the implementation of the above-mentioned control strategies requires a centralized controller, these control strategies are classified as centralized control strategies. To ensure good control performance, it is important to ensure accurate and timely communication between the central controller and the local controller. However, the inevitable communication delay and single point of failure will reduce the performance of the centralized control strategy and reduce the reliability of the microgrid system [16], [17].

B. Distributed Power Smoothing Control Strategies

Unlike the centralized control strategy, the distributed control strategy based on droop control relies only on local information, which avoids the need for communication between controllers and reduces the communication burden and computational burden of the system. By introducing virtual impedance in the droop control, the performance of the system, such as power distribution accuracy, can be significantly improved. Virtual impedance is a concept that utilizes the impedance relationship between voltage and current. It is an artificially introduced impedance added in the control process to simulate the existence of a virtual component. Unlike the actual impedance, the addition of virtual impedance does not cause additional losses to the power system, nor does it lead to any additional increase in engineering cost or equipment size. It also has the advantage of being able to reshape the output characteristics of the converter. Li et al. [18] combined adaptive droop control with adaptive virtual impedance, thereby achieving a reasonable power distribution among distributed power generation units.

In the *V-I* droop control-based strategy, the virtual resistance droop controller and virtual capacitor droop controller are applied to the battery and supercapacitor, respectively, to realize the power distribution between the two automatically. Xu et al. [19] added a SOC recovery loop to the supercapacitor control, which helps in the automatic recovery of the supercapacitor charge state and enables its continuous operation. In [20], the effect of line impedance on power distribution was discussed and the controller loop was designed accordingly. Voltage sags caused by droop coefficients are recovered in [21] and the control strategy is extended to multiple HESSs. For a cluster of energy storage units with high retarding rates, an integral droop control strategy was proposed by Lin et al. [22], whose coordinated control with the conventional *V-P* droop control strategy helps in transient power allocation in a decentralized manner in a single HESS. Zhang and Li [23] used virtual impedance loops to add virtual resistances and virtual capacitances in series between the converter and the dc bus, thus ensuring plug-and-play characteristics while decoupling the power flow between the supercapacitor and other distributed generation units.

Similar to *V-I* droop control, current-voltage (*I-V)* droop control is a widely used control method in microgrid applications, which uses the dc bus voltage as a feedback signal to achieve accurate current equalization. In [24], virtual impedance instead of constant droop coefficients in *I-V* droop control to achieve dynamic power sharing between batteries and supercapacitors. Gu et al. [25] used a frequency domain integer for the virtual output impedance of the ESS. The battery and supercapacitor absorb low-frequency and high-frequency power fluctuations, respectively, to coordinate time-scale and power-scale in distributed microgrid systems. In [26], a mode-adaptive decentralized control strategy was proposed to achieve power sharing between different power sources through dc bus voltage signals and formulate the microgrid's operation mode to achieve seamless conversion of control modes. Gao et al. [27] conducted a comparative study on *I-V* droop control and *V-I* droop control, focusing on steady-state power-sharing performance and stability. By deducing the output impedance and corresponding dynamic characteristics of the system, a generalized analytical impedance model is proposed to explore the stability of the system. Wang et al. [28] compared the dynamic response performance of *I-V* droop control and *V-I* droop control by establishing a state-space model. The advantages of *I-V* droop control in dynamic response are proved, and an adaptive PI controller is proposed, which can improve dynamic response and ensure good steady-state performance. Table I summarizes some power smoothing control strategies proposed in recent years and conducts a comparative analysis of their advantages and disadvantages.

With the advantages of no communication and low delay, the distributed control strategy has better control accuracy and lower implementation and operation difficulty in power smoothing control. It is also more suitable for the PPV application scenario under the shadow disturbance of vehicles.

TABLE I
CLASSIFICATION AND COMPARISON OF POWER SMOOTHING CONTROL STRATEGIES

Power smoothing control strategies		Ref.	Advantages	Disadvantages
Centralized control strategies	HPF/LPF	[7]	● Easy to implement	● A certain delay
	WT	[8]	● Good adaptability ● Simple control	● Depend on parameter selection
	EMD	[9]	● High adaptability ● Multitime-scale coordinated control	● Prone to modal aliasing
	SA	[10]	● Simple principle ● Good adaptability	● Depend on parameter selection
	MPC	[11]	● Strong constraint handling capability	● Highly dependent on model accuracy
	ANN	[13]	● Good autonomous learning ability ● Good fault tolerance	● Requires large amounts of data input
	FLC	[14]	● Able to handle uncertainties in the system	● Complex design ● Dependent on expert experience
Distributed control strategies	Traditional droop control	[18]	● No communication requirement ● Suitable for steady-state systems	● Difficult to achieve coordinated control among different energy storages
	Virtual impedance droop control	[24]	● No communication requirement ● Capable of achieving multiband decomposition	● Difficult to select virtual impedance parameters

TABLE II
PPV THREE-LEVEL HIERARCHICAL POWER SMOOTHING CONTROL STRUCTURE

	Inverter branch	Battery branch	Supercapacitor branch
Topological structure	Three-phase bridge inverter	Nonisolated bidirectional DC–DC converter	Nonisolated bidirectional DC–DC converter
Control strategy	Virtual impedance I-V droop control strategy (virtual inductance)	Virtual impedance I-V droop control strategy (virtual inductance and virtual resistance)	Virtual impedance I-V droop control strategy (virtual resistance)
Frequency division interval	Low frequency	Medium-low frequency	High frequency

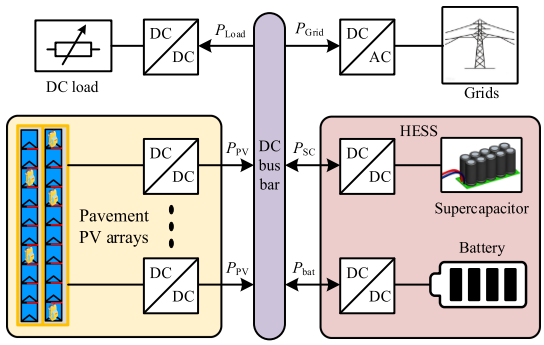

Fig. 1. Structure of DC microgrid.

However, the above-distributed control strategy only considers the power distribution within the hybrid energy storage and does not consider the inverter control link. In two-stage PV power generation systems, the inverter control link usually adopts a voltage-current double closed-loop control strategy, which delivers all the PV power to the grid stably by controlling the voltage of the dc bus. The virtual impedance droop control used in the ESS also takes the dc bus voltage as the control object. When the two work at the same time, the hybrid energy storage output will be interfered with by the inverter, which cannot achieve smooth control, and the inverter cannot absorb all the steady-state components of the PV power, resulting in a wrong power flow direction.

For this reason, the inverter control link will have to switch to other control strategies, such as the PQ control strategy [29], etc. At this time, to deliver all the steady state power in the PV power to the grid, the system will need to rely on communication to obtain power commands. Therefore, communication needs are introduced in this link, which makes the distributed control strategy of the HESS lose its greatest advantage. Once problems such as communication failures occur, the grid-connected inverter will lose the ability to deliver PV power in the event of a loss of power command. A large amount of energy is trapped on the dc bus, which will quickly consume the remaining capacity of the energy storage device, and then force the energy storage device to quit operation, resulting in system disassembly.

To solve the above-mentioned problems, based on the traditional virtual impedance droop control strategy, this article will apply the virtual impedance *I-V* droop control technology to the inverter control link, and then build a three-level hierarchical smoothing control strategy based on virtual impedance frequency division mechanism (TVID) to achieve smooth control of PV power fluctuations. Finally, the effectiveness of the proposed strategy is verified by simulation and experimental tests. The three-level hierarchical power smoothing control structure for PPV is shown in Table II.

The motivation and contributions of this article can be summarized as follows.

1) In a two-stage PPV power generation system with hybrid energy storage, the virtual impedance *I-V* droop control strategy is applied to the control of both the dc converter and the inverter. The similar *I-V* droop control structure can avoid the mutual interference in power distribution between the inverter and the hybrid energy storage.
2) The separate use of virtual resistance and virtual inductance can only achieve two-level frequency-domain hierarchical control. By combining virtual resistance and virtual inductance, an additional interval can be divided on the basis of the original two intervals, thereby achieving three-level frequency division. Through the establishment of the energy storage unit and the inverter closed-loop control model, the corresponding equivalent impedances for each branch were derived.
3) By introducing appropriate virtual impedances and adjusting the impedance characteristics of the three components, a three-level hierarchical power smoothing control can be achieved. The influence of the virtual impedance parameters of each branch on the system's frequency division mechanism was analyzed, providing a theoretical basis for the selection of virtual impedance parameters.
4) Through simulation tests under various working conditions, the smooth control of PV power under vehicle shadow disturbance is realized. Furthermore, a two-stage PV power generation system platform with hybrid energy storage was further built, and the LPF-HESS control strategy was compared on this platform. At the same time, a comparative experiment on energy storage technologies was conducted on the indoor PPV platform. The experimental results verified the effectiveness of the TVID control strategy in the field of PV power smoothing control.

The rest of this article is organized as follows. Section II introduces the two-stage PPV power generation system with hybrid energy storage. Section III describes TVID. Section IV gives the experimental procedure and the comparative analysis of the experimental results. Section V presents the conclusions drawn from the study.

II. TWO-STAGE PAVEMENT PV POWER GENERATION SYSTEM WITH HYBRID ENERGY STORAGE

A two-stage PPV grid-connected power generation system [30] can be regarded as a dc microgrid, as shown in Fig. 1, where the PV power and the alternating current (ac) grid are connected via a dc bus. Because of the volatility of PV power, it is usually necessary to incorporate energy storage devices to maintain the stability of the system power. The structure of the dc bus is convenient for the input and removal of the ESS and dc

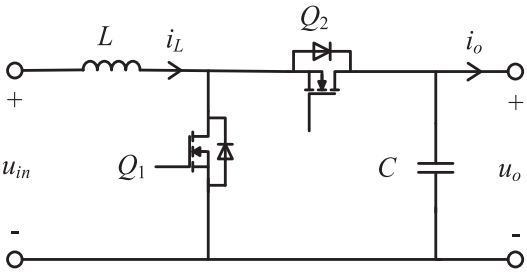

Fig. 2. Topology of bidirectional Boost converter.

load. To give play to the advantages of different energy storage devices and extend the service life of energy storage devices, HESSs of batteries and supercapacitors have been widely used.

The distinct characteristics of battery and supercapacitor in terms of energy density and power density determine the different roles they play in the system. The energy density of the battery is high, but its response speed is slow. It is difficult to address the high-frequency components in power fluctuations. Although the supercapacitor has a relatively good ability to respond quickly, its low energy density makes it unable to handle the low-frequency components in power fluctuations. The combined HESS made by combining the two components can precisely complement each other's advantages. It can effectively enhance the dynamic response capability of the system and extend the service life of the battery.

Under the action of vehicle shadow, the *P-V* output characteristic curve of the PPV array shows obvious multipeak characteristics. To investigate the trend of the PPV array's output curve with time. This article uses the perturb and observe method with a simple principle, high tracking accuracy, and strong stability to track the maximum power point of *P-V* characteristic curve.

The energy storage device plays the role of peak clipping and valley filling in the system, and its power flow requires bidirectional flow. In this article, a simple bidirectional Boost dc converter [31] is adopted to achieve this function. Fig. 2 shows its topology.

The small signal model of the bidirectional Boost converter is established by the state space averaging method

$$\begin{cases} L\frac{di_L}{dt} = du_{in} + (1-d)(u_{in}-u_0) = u_{in} - (1-d)u_o \\ C\frac{du_o}{dt} = d\cdot(-i_o) + (1-d)(i_L - i_o) = (1-d)i_L - i_o \end{cases} \tag{1}$$

where L represents the filter inductance; C represents the filter capacitance on the high voltage side; u_{in} represents the voltage of the converter's low voltage side, connecting the battery and the supercapacitor; u_o represents the voltage of the converter's high voltage side, which is connected to the dc bus; i_L represents inductor current; i_o represents current on the high voltage side; d represents the duty cycle of switch tube Q_1. Here the output is positive, and the real-time value of the electrical quantity is represented by a lower-case symbol.

The real-time variable can be decomposed into dc component and ac small signal component. The corresponding uppercase symbol represents its dc component, and the corresponding ac small signal component is marked with the symbol $\wedge$ based on the original. By separating the disturbance from (1) and ignoring the second-order small signal components, we can obtain

$$\begin{cases} L\frac{d\hat{i}_L}{dt} = \hat{u}_{\text{in}} - (1-D)\hat{u}_o + U_o\hat{d} & U_{\text{in}} = (1-D)U_o \\ C\frac{d\hat{u}_o}{dt} = (1-D)\hat{i}_L - I_L\hat{d} - \hat{i}_o & I_L = \frac{I_o}{1-D} \end{cases}. \tag{2}$$

The above-mentioned model is transformed into a frequency domain model by Laplace transform and then sorted out

$$\begin{aligned} \hat{i}_L &= \frac{I_0 + sCU_0}{s^2LC + D_p^2}\hat{d} + \frac{D_p}{s^2LC + D_p^2}\hat{i}_0 + \frac{sC}{s^2LC + D_p^2}\hat{u}_{\text{in}} \\ \hat{u}_0 &= \frac{U_0D_p - sLI_0/D_p}{sCU_0 + I_0}\hat{i}_L - \frac{U_0}{sCU_0 + I_0}\hat{i}_0 + \frac{I_0/D_p}{sCU_0 + I_0}\hat{u}_{\text{in}} \end{aligned} \tag{3}$$

where $D_p = 1 - D$ represents the duty cycle of the converter in steady state. The internal transformation relationship of the bidirectional Boost converter can be expressed as [32]

$$\begin{aligned} G_{il\_d} &= \frac{I_0 + sCU_0}{s^2LC + D_p^2} & G_{il\_io} &= \frac{D_p}{s^2LC + D_p^2} \\ G_{il\_uin} &= \frac{sC}{s^2LC + D_p^2} & & \\ G_{uo\_il} &= \frac{U_0D_p - sLI_0/D_p}{sCU_0 + I_0} & G_{uo\_io} &= \frac{-U_0}{sCU_0 + I_0} \\ G_{uo\_uin} &= \frac{I_0/D_p}{sCU_0 + I_0} & & \end{aligned} \tag{4}$$

where G_{il_d} represents the local transfer function of inductor current to duty cycle; G_{il_io} represents the local transfer function of inductor current to current on the high voltage side; G_{il_uin} represents the local transfer function of inductor current to voltage on the low voltage side; G_{uo_il} represents the local transfer function of voltage on the high voltage side to inductor current; G_{uo_io} represents the local transfer function of voltage on the high voltage side to current on the high voltage side; and G_{uo_uin} is the local transfer function of the voltage on the high voltage side to the voltage on the low voltage side.

III. Three-Level Hierarchical Smoothing Control Strategy Based on Virtual Impedance Frequency Division Mechanism

The ESS is connected to the PV system in the form of dc coupling through the dc bus, and its power flow relationship can be equated to the current relationship. Therefore, the main purpose of the control system is to achieve a reasonable distribution of internal current. The traditional droop control technology can only distribute the current in a fixed proportion. Even with the use of adaptive droop coefficients, it is impossible to achieve the effect of distributing the current according to the frequency domain. Therefore, the virtual impedance technology was integrated into this scheme.

In the proposed TVID, the battery, supercapacitor, and inverter all adopt virtual impedance droop control. By introducing suitable virtual impedance, the impedance characteristics of the

three are adjusted to achieve three-level hierarchical control. The PV grid-connected power can achieve automatic smoothing control, in which the stable and smooth power is transmitted to the ac power grid through the inverter. Medium and low frequency power fluctuations are absorbed by the battery. High frequency power fluctuations are quickly responded by the supercapacitor. There is no need for communication between the subsystems. There is no need for complex signal processing technology, which greatly reduces the communication and calculation pressure of the system. Fig. 3 shows the TVID control strategy system block diagram.

In the HESS composed of a battery and a supercapacitor, the introduction of virtual inductance enables the battery to have integral characteristics in the droop control. It can absorb the low-frequency components of power fluctuations. The introduction of virtual resistance enables the supercapacitor to have proportional characteristics in the droop control, which is suitable for responding to high-frequency power changes [24]. When the inverter branch is connected to the frequency division system, the original two-level frequency division needs to be refined into three-level frequency division. That is, through impedance shaping, the impedances of the three branches respectively act in the low-frequency, medium-frequency, and high-frequency regions. In this strategy, the supercapacitor droop control loop still adopts a virtual resistance to maintain its dominant role in the high frequency interval and absorb the high-frequency power fluctuation. Virtual inductance is used in the inverter droop control loop to achieve the leading role in the ultra-low frequency interval (frequency approaching 0 Hz), and smooth power input to the grid. Virtual resistance and virtual inductance are applied simultaneously in the battery droop control loop to achieve the leading role in the medium and low frequency interval and absorb the residual power fluctuation.

According to the *I-V* droop control characteristics, the current relationship of the three-branch input dc bus is as follows:

$$\begin{aligned} i_{\text{o\_inv\_ref}} &= (U_{\text{dc\_ref}} - u_{\text{dc}})\,\frac{1}{sL_{\text{inv}}} \\ i_{\text{o\_bat\_ref}} &= (U_{\text{dc\_ref}} - u_{\text{dc}})\,\frac{1}{R_{\text{bat}} + sL_{\text{bat}}} \\ i_{\text{o\_SC\_ref}} &= (U_{\text{dc\_ref}} - u_{\text{dc}})\,\frac{1}{R_{\text{SC}}} \end{aligned} \tag{5}$$

where $i_{o\_\text{inv\_ref}}$ represents the current reference value of the inverter flowing into the dc bus; $i_{o\_\text{bat\_ref}}$ represents the current reference value of the battery injected into the dc bus; $i_{o\_\text{SC\_ref}}$ represents the current reference value of the supercapacitor injected into the dc bus; $U_{\text{dc\_ref}}$ represents the dc bus voltage reference value; u_{dc} represents the bus voltage; L_{inv} represents the virtual inductance introduced in the inverter droop controller; L_{bat} indicates the virtual inductance introduced in the battery droop controller; R_{bat} indicates the virtual resistance introduced in the battery droop controller; and R_{sc} indicates the virtual resistance introduced in the supercapacitor droop controller.

Thus, a second-order current filter composed of three branches can be further obtained: (6) shown at the bottom of this page, where i_{o_inv} represents the actual current of the inverter flowing into the dc bus; i_{o_bat} represents the actual current of the battery injected into the dc bus; i_{o_SC} represents the actual current of the supercapacitor injected into the dc bus.

Through the appropriate parameter setting, the three-level hierarchical control of ultra-low frequency, medium and low frequency, and high frequency can be achieved. However, the above-mentioned filter regards the virtual impedance as the branch impedance of the controller where it is located. It is different from the actual branch impedance. Therefore, it is necessary to further analyze the system impedance characteristics under the TVID control strategy.

The *I-V* droop control strategy is used in the energy storage converter, where the outer loop is the bus voltage droop control loop, which outputs the command value of the inductor current required for the inner loop. The inner loop achieves converter control by tracking the command value of the inductor current, and the closed-loop small-signal model is shown in Fig. 4.

The closed-loop transfer function of the current inner loop in this model is

$$T_{c1} = \frac{G_{pi}G_{il\_d}}{1 + G_{pi}G_{il\_d}} \tag{7}$$

where G_{pi} represents the transfer function of the proportional integral (PI) controller.

The closed-loop transfer function controlling the outer loop is

$$T_{c2} = \frac{G_{uo\_il}T_{c1}}{Z_v D_p + G_{uo\_il}T_{c1}} \tag{8}$$

where Z_v represents virtual impedance.

The external impedance characteristics of the dc bus side are as

$$Z_o = Z_v D_p T_{c2}\left(\frac{G_{il\_io}}{G_{pi}G_{il\_d}} + \frac{G_{uo\_io}}{G_{uo\_il}T_{c1}}\right). \tag{9}$$

To construct impedance characteristics similar to the energy storage branch droop controller. This article improved the voltage and current double closed-loop control strategy commonly used in inverter control and replaced the voltage outer loop with the *I-V* droop control structure. The inner loop control

$$\begin{aligned} i_{\text{o\_inv}} &= G_{\text{inv}}(s)\cdot i_{\text{o}} = \frac{L_{\text{bat}}R_{\text{SC}}s + R_{\text{bat}}R_{\text{SC}}}{L_{\text{inv}}L_{\text{bat}}s^2 + (R_{\text{bat}}L_{\text{inv}} + R_{\text{SC}}L_{\text{inv}} + L_{\text{bat}}R_{\text{SC}})s + R_{\text{bat}}R_{\text{SC}}}\cdot i_{\text{o}} \\ i_{\text{o\_bat}} &= G_{\text{bat}}(s)\cdot i_{\text{o}} = \frac{R_{\text{SC}}L_{\text{inv}}s}{L_{\text{inv}}L_{\text{bat}}s^2 + (R_{\text{bat}}L_{\text{inv}} + R_{\text{SC}}L_{\text{inv}} + L_{\text{bat}}R_{\text{SC}})s + R_{\text{bat}}R_{\text{SC}}}\cdot i_{\text{o}} \\ i_{\text{o\_SC}} &= G_{\text{SC}}(s)\cdot i_{\text{o}} = \frac{L_{\text{inv}}L_{\text{bat}}s^2 + R_{\text{bat}}L_{\text{inv}}s}{L_{\text{inv}}L_{\text{bat}}s^2 + (R_{\text{bat}}L_{\text{inv}} + R_{\text{SC}}L_{\text{inv}} + L_{\text{bat}}R_{\text{SC}})s + R_{\text{bat}}R_{\text{SC}}}\cdot i_{\text{o}}. \end{aligned} \tag{6}$$

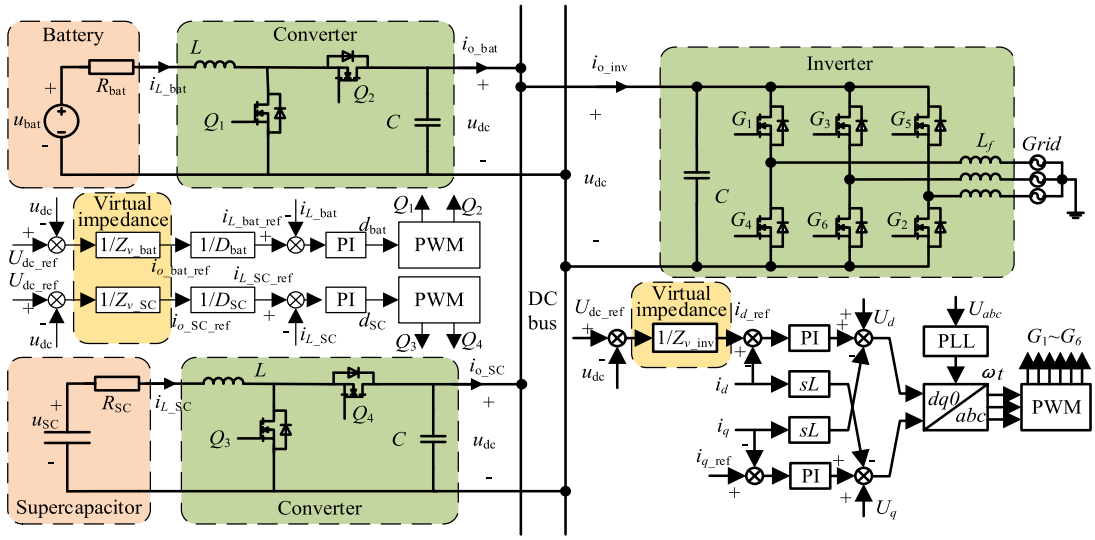

Fig. 3. System block diagram of a three-level hierarchical smoothing control strategy based on virtual impedance droop control.

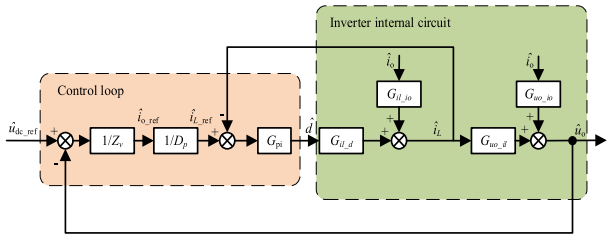

Fig. 4. Small-signal model for virtual impedance-based *I-V* droop control.

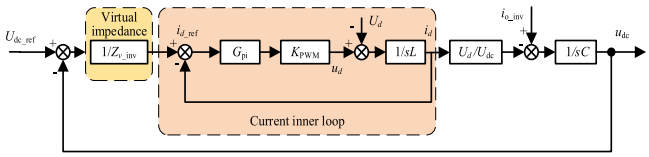

Fig. 5. Equivalent control block diagram of inverter based on virtual impedance *I-V* droop control.

structure remained unchanged, and its control object was still *d*-axis current. The *I-V* droop control strategy of the inverter based on virtual impedance is constructed. In the *dq* coordinate system, the initial position of the *d*-axis is ordered to coincide with A-phase to ensure that the *q*-axis component of the ac voltage is always zero, thus simplifying the analysis. Therefore, the *d*-axis control loop is mainly discussed here. Fig. 5 shows the equivalent control block diagram of the *I-V* droop controller of the inverter based on virtual impedance.

By simplifying the control block diagram, the transfer function of the inner current loop can be obtained as follows:

$$T_{c\_id} = \frac{G_{\text{pi}} K_{\text{PWM}}}{sL + G_{\text{pi}} K_{\text{PWM}}} \tag{10}$$

where K_{PWM} represents the pulsewidth modulation (PWM) gain coefficient.

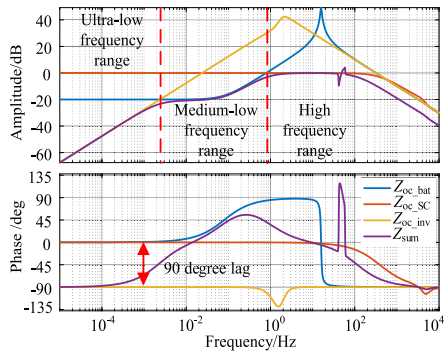

Fig. 6. Bode diagram of branch impedance characteristics after phase correction.

The transfer function of the outer voltage loop is

$$T_{v\_udc} = \frac{T_{c\_id} U_d}{sCZ_{v\_\text{inv}} U_{\text{dc}} + T_{c\_id} U_d} \tag{11}$$

where U_d represents the *d*-axis component of the grid side voltage; Z_{v_inv} represents the virtual impedance introduced in the inverter droop control; U_{dc} represents the dc component of the bus voltage.

The equivalent impedance of the inverter is

$$Z_{\text{o\_inv}} = \frac{u_{\text{dc}}}{i_{\text{o\_inv}}} = \frac{U_{\text{dc}}}{U_d} \frac{T_{v\_udc}}{T_{c\_id}} Z_{v\_\text{inv}}. \tag{12}$$

The impedance characteristics of the three branches can be calculated by substituting the above-mentioned impedance design scheme into (9) and (12), respectively. Fig. 6 shows the impedance characteristics of each branch. It can be seen that in the ultra-low frequency region, the parallel impedance characteristic Z_{sum} is dominated by the inverter branch impedance Z_{oc_inv}. In the medium- and low-frequency region, the parallel impedance characteristic Z_{sum} is dominated by the battery branch impedance Z_{oc_bat}. In the high-frequency region, the

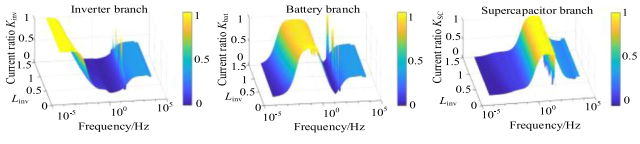

Fig. 7. Three-dimensional diagram of the influence about virtual inductance L_{inv} on current distribution characteristics.

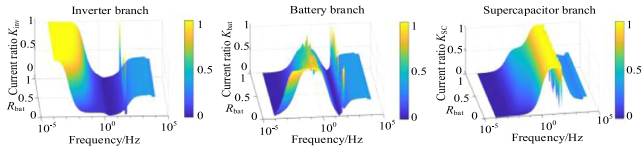

Fig. 8. Three-dimensional diagram of the influence about virtual resistance R_{bat} on current distribution characteristics.

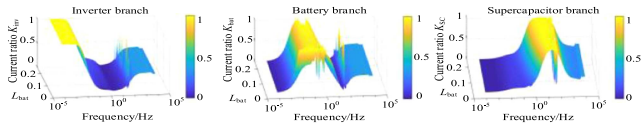

Fig. 9. Three-dimensional diagram of the influence about virtual inductance L_{bat} on current distribution characteristics.

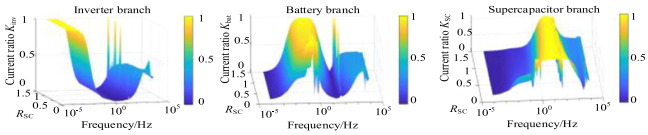

Fig. 10. Three-dimensional diagram of the influence about virtual resistance R_{SC} on current distribution characteristics.

parallel impedance characteristic Z_{sum} is dominated by the supercapacitor branch impedance Z_{oc_SC}. Dominance means that the bus current in this frequency interval will mainly flow to this branch.

According to the parallel impedance relationship, the current distribution characteristics of each branch can be calculated as follows:

$$K_{\text{inv}} = \frac{Z_{\text{oc\_bat}} Z_{\text{oc\_SC}}}{Z_{\text{oc\_bat}} Z_{\text{oc\_SC}} + Z_{\text{oc\_inv}} Z_{\text{oc\_bat}} + Z_{\text{oc\_inv}} Z_{\text{oc\_SC}}}$$
$$K_{\text{bat}} = \frac{Z_{\text{oc\_inv}} Z_{\text{oc\_SC}}}{Z_{\text{oc\_bat}} Z_{\text{oc\_SC}} + Z_{\text{oc\_inv}} Z_{\text{oc\_bat}} + Z_{\text{oc\_inv}} Z_{\text{oc\_SC}}}$$
$$K_{\text{SC}} = \frac{Z_{\text{oc\_inv}} Z_{\text{oc\_bat}}}{Z_{\text{oc\_bat}} Z_{\text{oc\_SC}} + Z_{\text{oc\_inv}} Z_{\text{oc\_bat}} + Z_{\text{oc\_inv}} Z_{\text{oc\_SC}}} \quad (13)$$

where K_{inv} represents the current distribution characteristics of the inverter branch; K_{bat} represents the current distribution characteristics of the battery branch; and K_{SC} represents the current distribution characteristics of the supercapacitor branch.

Fig. 7 shows a three-dimensional (3-D) diagram of the influence of virtual inductance L_{inv} of the inverter droop controller on the current distribution characteristics. It can be seen that the current distribution characteristics of the three branches are significantly different in the frequency interval. The current distribution characteristic ratio of the inverter branch is mainly concentrated in the range below 0.01 Hz and the current distribution ratio in the range is close to 1. Within this ultra-low frequency interval, the current fluctuation is very slow, which means that the power fluctuation of the inverter transmission is very small, so it meets the power smoothing control requirements required by this strategy. The current distribution characteristic of the battery branch is close to 1 in the range of 0.01–1 Hz, which indicates that the battery has a strong absorption effect on the current in this medium- and low-frequency interval. The current distribution characteristic of the supercapacitor branch has a high amplitude in the range of 1–100 Hz, which mainly acts on the absorption of high-frequency current.

From the trend of current distribution characteristics in Fig. 7, it can be seen that the effect of virtual inductance L_{inv} is mainly reflected in the junction region between the ultra-low frequency interval and the medium- and low-frequency interval. There is no significant change in the characteristics of other frequency domain intervals. As the virtual inductance L_{inv} increases, more low-frequency current is transferred from the inverter branch to the battery branch, which will make the power of the inverter branch smoother, while the battery branch has to bear more low-frequency components. Figs. 8 –10, respectively, show the 3-D diagrams of the impact trend of the battery droop controller virtual resistance R_{bat}, the battery droop controller virtual inductance L_{bat}, and the supercapacitor droop controller virtual resistance R_{SC} on current distribution characteristics.

The effect of virtual resistance R_{bat} is opposite to the effect of virtual inductance L_{inv}. With the increase in resistance, more and more medium and low frequency components are transferred from the battery branch to the inverter branch, and this trend gradually becomes stable after increasing to 0.4. At the same time, this parameter also has a certain effect on the boundary of the medium and low frequency region and high-frequency region. Part of the high-frequency component is transferred from the supercapacitor branch to the battery branch. The influence of virtual inductance L_{bat} is concentrated at the junction of the medium and low frequency region and high-frequency region. With the increase of virtual inductance, more medium and low frequency components are gradually included in the absorption range of the supercapacitor branch.

The main effect of the above-mentioned several parameters is to act on one side of the boundary of a certain interval, while the virtual resistance R_{SC} acts on both sides of the boundary of the high-frequency interval. With the increase of its virtual resistance, both sides of the boundary of the high-frequency interval dominated by the supercapacitor branch all shrink, and the absorption range of the branch to the high-frequency component decreases gradually.

IV. Simulation Testing

To verify the effectiveness of the proposed TVID control strategy, a simulation model of a PPV storage power generation system with a bus voltage of 600 V and rated output power of 5.1 kW was built based on the MATLAB/Simulink platform.

TABLE III
SIMULATION PARAMETERS OF PPV ENERGY STORAGE POWER GENERATION SYSTEM

	Parameter	Value
Voltage classes	DC bus voltage u_{dc}	600 V
	Three-phase AC network	220 V
PV array	Number of series	10
	Number in parallel	2
	Rated power	5.1 KW
Battery	Rated capacity	5.1 Ah
	Rated voltage	240 V
Supercapacitor	Rated capacitance	10 F
	Rated voltage	300 V
Virtual impedance default parameter	Virtual inductance L_{inv}	1
	Virtual inductanceL_{bat}	0.1
	Virtual resistance R_{bat}	0.1
	Virtual resistance R_{SC}	1

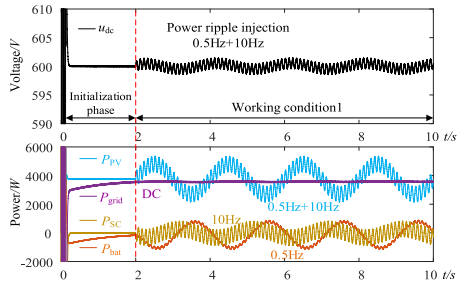

Fig. 11. Simulation waveform of DC bus voltage and branch power in case 1.

The system consists of four submodules, the PV module adopts a Boost converter, the battery module, and the supercapacitor module adopts a bidirectional dc converter. They are connected in parallel to the inverter module via the dc bus. The specific system simulation parameters are shown in Table III.

In case 1, the ripple absorption characteristics of the system for different frequencies are tested by adding the power ripple of certain frequencies. Fig. 11 shows the simulation waveform of dc bus voltage and branch power in case 1.

During t = 0–2 s, the system is starting, the light intensity is maintained at 750 W/m^2, and the PV power P_{PV} is stable at 3.75 kW. Between t = 2 and 10 s, the light intensity of the PV module increases by 200 W/m^2, and the PV output contains sinusoidal ripples at frequencies of 0.5 Hz and 10 Hz. Under the proposed TVID, power smoothing control was achieved.

In case 2, the PV output is designed as a rectangular wave to test the working state of the system under the state of power surge and power drop.

Fig. 12 shows the simulation waveform of dc bus voltage and branch power changing with the virtual impedance L_{inv} in case 2. After the start-up phase, the PV output adds a rectangular wave component based on the constant power of 3.75 kW, whose maximum and minimum values are 5.08 kW and 2.42 kW, respectively. And the power sudden change value $\Delta P = 2.66$ kW, reaching 50% of the rated power of the system. Considering that

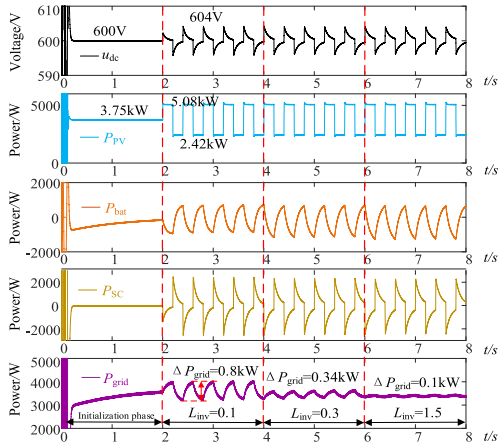

Fig. 12. Simulation waveform of DC bus voltage and branch power varying with virtual impedance L_{inv} in case 2.

the frequency of power fluctuations is much higher in the PPV usage scenario than in other application scenarios. Therefore, the power change frequency is set to 5 Hz, which means that each transient response time is only 0.2 s. Some parts of the system, such as the inverter module, pursue a slow response speed to absorb smooth power, and it is difficult to achieve the final steady state under such conditions. However, testing the system performance under such extreme conditions is the significance of the existence of this case.

In Fig. 12, the virtual inductance L_{inv} is set to 0.1, 0.3, and 1.5, which operate in the three time periods t = 2–4 s, 4–6 s, and 6–8 s, respectively. As the virtual impedance introduced in the inverter branch, its most significant influence is reflected in the grid-connected power P_{grid} waveform. As the virtual inductance L_{inv} increases from 0.1 to 0.3, the power fluctuation peak value of P_{gird} decreases from 0.8 to 0.34 kW, and the grid-connected power fluctuation decreases significantly. Finally, when the L_{inv} increases to 1.5, the peak value of power fluctuation is only 0.1 kW, which is slightly larger than the switch ripple, and a good smooth control effect is achieved. This part of the reduced fluctuation power is allocated to the energy storage branch, so it almost does not affect the state of the dc bus voltage u_{dc}, and its voltage fluctuation is always maintained at the peak of 604 V. The simulation results are consistent with the theoretical analysis of the virtual inductance parameter L_{inv} in Fig. 7, which verifies the validity of the theoretical analysis. It is worth noting that although the increase of virtual inductance L_{inv} will improve the grid-connected power fluctuation, it will also cause the response speed of the inverter branch to be too slow, such as the startup stage is set because of the slow response of the inverter branch. With the increase of parameters, the problem is more and more significant, too slow response speed will occupy more capacity of the energy storage device.

Fig. 13 shows the simulation waveform of the dc bus voltage and branch power changing with the virtual impedance R_{SC} in case 2. The study object is replaced by the virtual resistance R_{SC}, whose parameter values in the three time periods are 1, 2, and 3, respectively. With the increase of virtual resistance, the medium

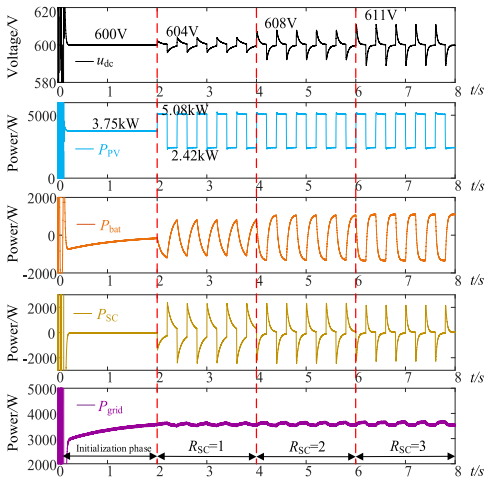

Fig. 13. Simulation waveform of DC bus voltage and branch power varying with virtual impedance R_{SC} in case 2.

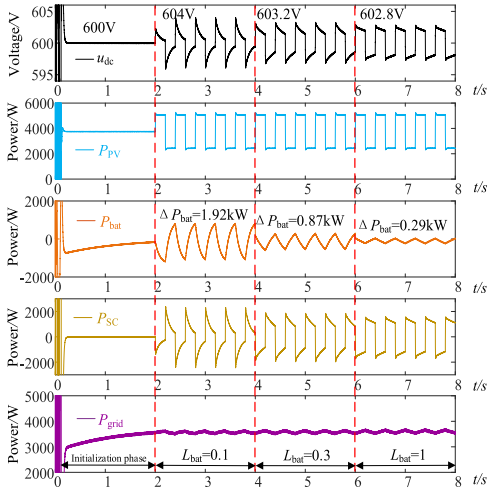

Fig. 14. Simulation waveform of DC bus voltage and branch power varying with virtual impedance L_{bat} in case 2.

and low frequency power in the supercapacitor branch gradually decreases, which is directly reflected in that the supercapacitor power P_{SC} recovers to a position closer to 0 in the same time after each power sudden change. The corresponding battery branch is also affected by it, and its power response speed is greatly increased after the sudden change, indicating that it bears more medium- and high-frequency components. In the analysis shown in Fig. 10, as the virtual resistance increases, the boundaries on both sides of the frequency interval dominated by the supercapacitor branch shrink. This shows that in addition to the above-mentioned effects, the high-frequency power absorbed by the supercapacitor also decreases, and this part of the power is not within the bearing range of other branches. It can only be retained on the dc bus and absorbed by the filter capacitor. The fluctuation peak of dc bus voltage u_{dc} increases from 604 to 608 V and 611 V. However, the virtual resistance R_{SC} is not the smaller the better, the too small resistance value will make the supercapacitor bear too much medium and high frequency components, and occupy a large amount of capacity. Its state of charge is more likely to reach the critical position, affecting the long-term operation of the supercapacitor.

Figs. 14 and 15, respectively, show the simulation waveforms of dc bus voltage and branch power changing with virtual impedance L_{bat} and R_{bat} under case 2. Fig. 14 shows the operating state of the system when the virtual inductance L_{bat} is 0.1, 0.3, and 1, respectively. Fig. 15 shows the operating state of the system when the virtual resistance R_{bat} is 0.1, 1, and 2, respectively. The effects of virtual impedance L_{bat} and R_{bat} on the system are similar, which are mainly reflected in the battery branch power P_{bat} and the supercapacitor branch power P_{SC}. With the increase of both, the dc bus voltage fluctuation peak value decreases slightly.

In case 3, the ordinary PV array is replaced by a two-lane PPV array. The complex output characteristics of the actual PPV scene are simulated by the vehicle shadow model based on cellular automata. In this model, the vehicle position information is updated every 0.05 s. When there is no vehicle shading, the

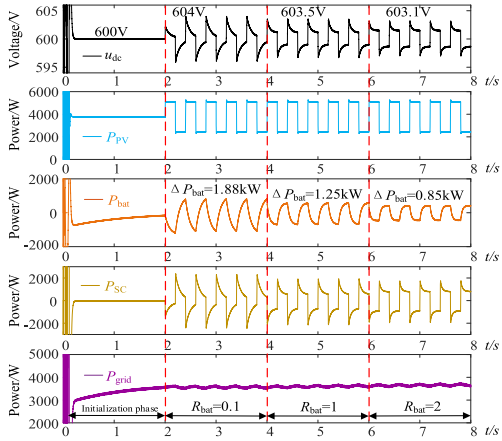

Fig. 15. Simulation waveform of DC bus voltage and branch power varying with virtual impedance R_{bat} in case 2.

light intensity of the PV cell is 1000 W/m^2 by default. When the vehicle shadow moves to the top of the PV module, it is regarded as full plane coverage and the light intensity is 200 W/m^2. Fig. 16 shows the simulation waveform of the power smoothing control of the PPV array under the shadow of a dynamic vehicle.

As can be seen from the PPV output in Fig. 16(a), under the action of rapidly updated vehicle shading, PV power fluctuates very sharply. The maximum value of power drop exceeds 60% of the rated power, and the duration of power drop occurs randomly between 0.05 and 0.2 s. Such violent fluctuations also increase the difficulty of transient control of PV converters, resulting in a large number of high-frequency ripples in PV output power.

Fig. 16(b) shows the simulation waveform of A-phase grid-connected current i_a. The total harmonic distortion (THD) at $t = 1$ s and $t = 2$ s is 15.2% and 4.79%, respectively. The problem of low grid-connection quality under the interference of control strategy is proved. However, THD at $t = 8$ s is only 0.88%, which verifies the great advantage of the proposed control strategy in grid-connected quality.

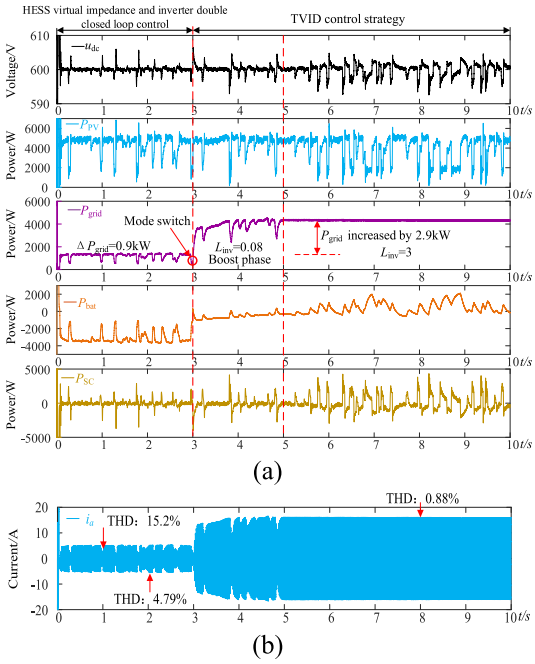

Fig. 16. Simulation waveform of PPV array power smoothing control under vehicle shadow disturbance in case 3. (a) Power simulation waveform of each branch. (b) Grid-connected current.

V. Experimental Verification

This section sets up a two-stage PV power generation system platform with hybrid energy storage, and verifies the effectiveness and practicability of the TVID control strategy proposed in this article in the field of PV power smooth control.

A. Power Smoothing Control Under Output of PV Simulator

The PV power generation system platform is composed of PV, battery, supercapacitor and inverter in parallel. In this experiment, PV simulator Agilent E4360A is used to simulate the output of PV array. The Boost converter required by the PV unit can be replaced by a bidirectional dc–dc converter. So the bidirectional dc–dc converter is used as the power conversion unit of the PV array, battery, and supercapacitor. The main function of the inverter branch is to achieve smooth absorption of PV power. Grid-connected control of the inverter is not the focus of this article, so the ac power grid is replaced by a 5-Ω three-phase resistance load to absorb PV power. The experimental platform is shown in Fig. 17, and the topology diagram is shown in Fig. 1.

In this experiment, the dc bus voltage is set to 60 V, and the specific parameters are shown in Table IV.

The PV power fluctuation characteristic is realized by setting the PV voltage command as a rectangular wave, in which the high and low levels are 38 and 32 V, respectively. The rising edge corresponds to the sudden drop in PV power, the falling edge corresponds to the sudden rise in PV power, and the switching frequency of high and low levels is 0.2 s. The power input characteristic in the form of a rectangular wave can simulate the worst power fluctuation condition (power sudden change), test the control effect of the system in extreme conditions such as power sudden change, and reflect the current frequency division characteristic well.

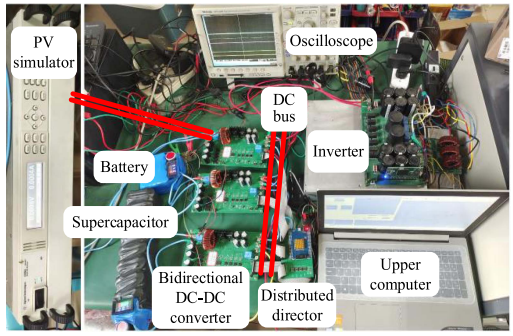

Fig. 17. Experimental platform under PV output is simulated by PV simulator.

TABLE IV
PV Simulator Experimental Platform Parameters

	Parameter	Value
PV characteristic curve	Maximum power point voltage	32 V
	Maximum power point current	3.5 A
	Open circuit voltage	40 V
	Short circuit current	4 A
Battery	Rated capacity	4.4 Ah
	Normal working voltage	34-38 V
Supercapacitor	Rated capacitance	27 F
	Safe working voltage	15-40 V

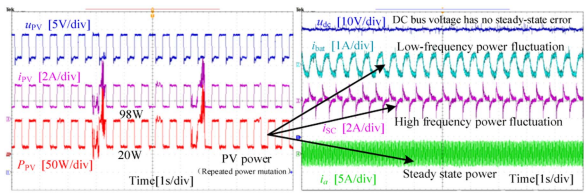

Fig. 18. System experiment waveform under the input of PV simulator.

Fig. 18 shows the dc bus voltage and current waveform of each branch during the operation of the TVID control strategy. The fluctuation state of dc bus voltage can reflect the overall stability of the system. The branch current is positively correlated with the branch power, which can directly reflect the frequency division absorption effect of PV power fluctuation. In the process of frequent PV power sudden change, the dc bus voltage is always better maintained near 60 V, indicating that the system still has strong stability under extreme conditions such as power sudden change. The battery branch current i_{bat} changes back and forth on both sides of the 0 value, and the steady state component is almost 0, indicating that the absorbed power does not contain the dc component.

In the existing distributed PV power smoothing control strategy, only the power frequency division mechanism inside the hybrid energy storage is considered. The inverter branch still needs to rely on communication to obtain power instructions, which cannot achieve real distributed control. Therefore, the HESS based on a low-pass filter (LPF-HESS), which is more common in centralized control strategies, is used for comparative experiments. Fig. 19 shows the experimental waveforms of

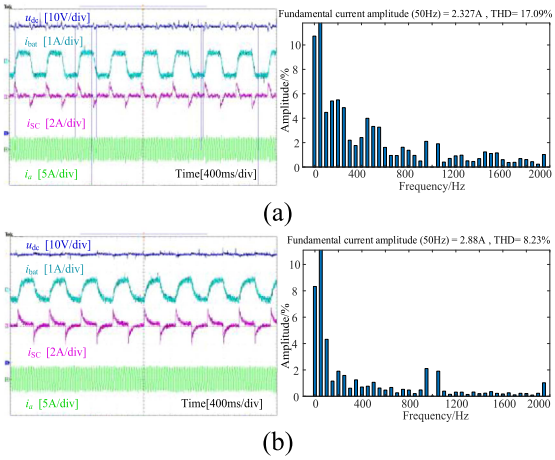

Fig. 19. Experimental waveforms comparing LPF-HESS and TVID. (a) LPF-HESS control policy. (b) TVID control policy.

comparison between the LPF-HESS control strategy and the TVID control strategy.

It can be seen that both of them realize the frequency division absorption of power fluctuations by hybrid energy storage, and the power absorbed by the inverter branch has a better smoothness. However, the difference is that the voltage fluctuation of the dc bus under the LPF-HESS control strategy is more significant, and the current THD reaches 17.09%. This is due to the delay effect caused by sampling, calculation, filtering, communication, control, etc., which makes the energy storage device respond too slowly to the transient component of the power sudden change. The energy that does not respond in time is trapped in the dc bus, which causes the voltage fluctuation of the dc bus, and then affects the inverter current. In contrast, the TVID control strategy does not need filtering calculation and communication, which greatly reduces the control delay and has a faster response to the transient component. Therefore, the dc bus voltage fluctuation is smaller, and the current THD is only 8.23%, which is much lower than the LPF-HESS control.

B. Power Smoothing Control of Pavement PV Under Vehicle Shadow Disturbance

To deeply explore the influence of vehicle shadow disturbance on PV output, a PPV system experiment platform is built. The platform includes PV arrays, car models that simulate real vehicles, and stage lights that simulate different light intensifies and angles. With the movement of the vehicle, the vehicle shadow will produce an irregular mask on the PPV, resulting in the PV output showing randomness and volatility. The construction of the PPV platform provides a strong support for the verification of the subsequent power smoothing control strategy. The indoor PPV platform is shown in Fig. 20.

The PV power generation system platform is composed of an indoor PPV, a battery, a supercapacitor and a load in parallel. The bidirectional dc–dc converter continues to be used as a power conversion unit for PV array, battery, and supercapacitor. The experimental platform is shown in Fig. 21.

Fig. 20. Indoor PPV with vehicle shadow disturbance.

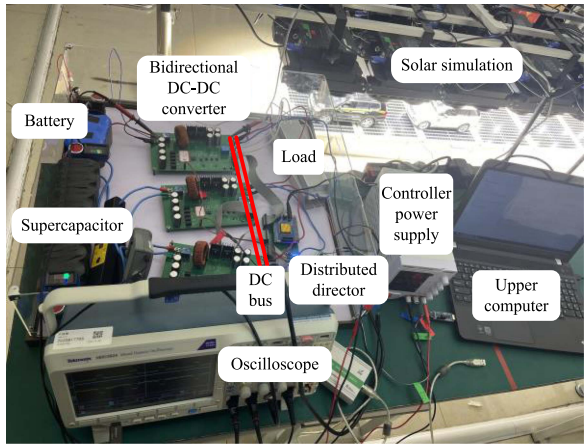

Fig. 21. Experimental platform of indoor PPV system.

TABLE V
INDOOR PPV EXPERIMENTAL PLATFORM PARAMETERS

	Parameter	Value
Solar simulation	Illumination intensity	1000 W/m²
PV array	Number of series	2
	Number in parallel	3
	Rated power	120 W
PV characteristic curve	Maximum power point voltage	34 V
	Maximum power point current	1.9 A
	Open circuit voltage	46 V
	Short circuit current	2.4 A

In this experiment, the dc bus voltage is set to 50 V. The parameters of the battery and supercapacitor remain unchanged. The PV characteristics curve of the PPV system was measured using the MP170 instrument. The specific parameters are shown in Table V.

When a vehicle passes by, the PPV is in a local shade state, and the maximum power point tracked by the maximum power point tracking algorithm changes, making the corresponding PV output voltage reduced to about 20 V, and the curve presents multipeak characteristics. When the vehicle passes through, the PPV restores to the unobstructed state, and the PV output voltage returns to the maximum power point voltage of 32 V. With the vehicle entering and leaving, the PV output curve under the vehicle shadow disturbance presents the characteristics of up and down mutation, which fully and truly restores the actual pavement conditions. Fig. 22 shows the waveforms of PV output voltage u_{PV}, dc bus voltage u_{dc}, battery branch current i_{bat} and

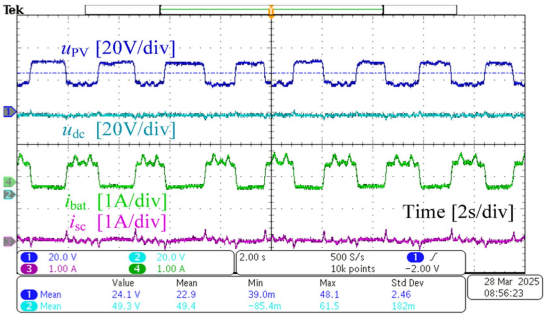

Fig. 22. System experiment waveform of PPV smoothing control strategy under vehicle shadow disturbance.

supercapacitor branch current i_{sc} during the operation of the TVID control strategy. The curves are represented by blue, cyan, green, and purple, respectively.

With the continuous shuttle of the vehicle, the PV output power fluctuates frequently. But even so, the dc bus voltage is always maintained within the rated range of $\pm 1\%$, with minimal ripple. This shows the effectiveness of the power smoothing control strategy.

The relationship between the current curve of the battery branch and the PV output curve is approximately mirrored to maintain the dynamic balance of the system power. At the same time, the low frequency component of the fluctuating power is absorbed. The branch current of the supercapacitor is centered on the zero value and fluctuates rapidly and frequently in both directions, with the dc component approaching zero. This characteristic is consistent with the theoretical frequency domain interval in which the supercapacitor is responsible for absorbing high-frequency power fluctuations in the strategy. The results show that the supercapacitor can respond quickly to the rapid change of power and effectively suppress the high-frequency power fluctuation. And through the mutual cooperation with the battery, it can jointly ensure the stable operation of the system.

In actual industrial PV applications, due to cost and complexity constraints, a single battery ESS remains the commonly adopted solution at present. Therefore, the commonly used single battery energy storage was adopted for the comparative experiment. Fig. 23 shows the comparison experiment waveforms of single battery energy storage and hybrid energy storage.

It can be seen that both have achieved power smoothing control. However, the difference lies in that the fluctuation of the dc bus in the battery energy storage is more significant. Moreover, the number of tiny spike fluctuations is much greater than that in the hybrid energy storage. This is because the battery simultaneously undertakes the dual tasks of compensating for the PV output and absorbing power fluctuations. In scenarios where the PV power fluctuations are not significant, a single battery can meet the demand for power smoothing. However, in scenarios with frequent shadow disturbances, when dealing with the high-frequency components within the power fluctuations, the battery, due to its own characteristics, has difficulty effectively handling such high-frequency fluctuations. This results in the portion of the high-frequency component that is not adequately responded to being trapped in the dc bus, causing the dc

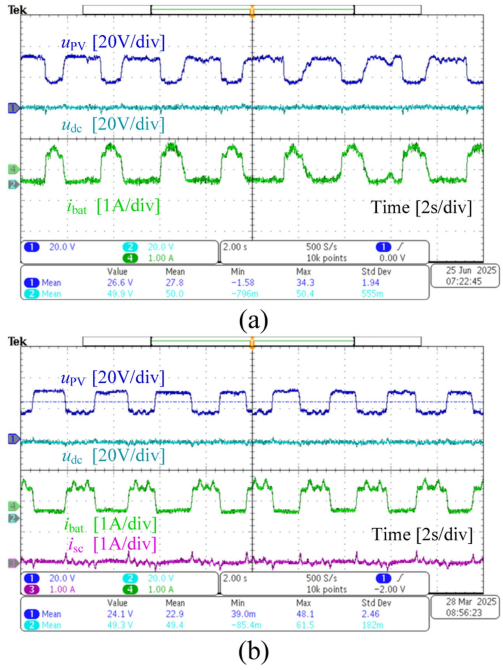

Fig. 23. Experimental waveforms comparing battery energy storage and hybrid energy storage. (a) Battery energy storage. (b) Hybrid energy storage.

bus to exhibit multiple tiny spike fluctuations. In contrast, hybrid energy storage can help the battery to share the task of absorbing power fluctuations because of the addition of the supercapacitor. And based on TVID, the power fluctuation can be absorbed in frequency division, thus reducing the burden of the battery. In addition, the battery will absorb power fluctuations regardless of whether it is charging or discharging. In a HESS, the battery only needs to absorb low-frequency fluctuations. The longer-lasting supercapacitor will undertake more charging and discharging task. Therefore, the current curve of the battery in battery energy storage shows more frequent fluctuations compared to that of hybrid energy storage.

In complex traffic scenarios where vehicles continue to shuttle, each branch current responds quickly and accurately to fluctuations in PV power. It can adjust the change trend in time according to the change of PV output, which is the advantage of distributed control strategy. The dc bus voltage curve in battery energy storage shows multiple tiny high-frequency spikes. This is because a single battery cannot fully absorb high-frequency power fluctuations, resulting in some high-frequency components remaining in the dc bus. At the same time, with the addition of a supercapacitor, the deviation of the dc bus voltage in the hybrid energy storage from the rated value is 50 ± 0.7 V, so there is no obvious voltage fluctuation. This phenomenon further verifies the effectiveness of the power smoothing control strategy proposed in this article, and proves that the strategy can ensure the stable operation of the system under long and complex working conditions. Fig. 24 shows the waveforms of the experiment with longer observation intervals. The observed parameters are unchanged.

In summary, in the scenario of vehicle shuttle, PV output presents sudden and random changes up and down. The

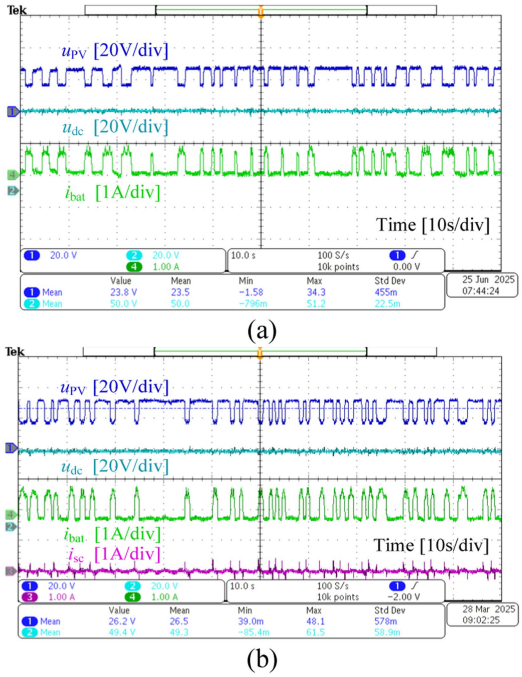

Fig. 24. Experimental waveforms comparing under long time disturbance of vehicle shadow. (a) Battery energy storage. (b) Hybrid energy storage.

HESS composed of battery and supercapacitor absorbs the low-frequency and high-frequency components of fluctuating power respectively according to its own characteristics. The system can achieve smoothing control of distributed PV power without communication support.

VI. Conclusion

This article proposes a three-level hierarchical smoothing control strategy based on the virtual impedance frequency division mechanism. The virtual impedance droop control technology is applied to the two-stage PPV power generation system. By constructing the impedance characteristics of the system, the frequency division absorption characteristics of three parallel branches are realized. Without communication, it can realize the automatic absorption of the steady-state component of the PPV power. At the same time, the hybrid energy storage characteristics are utilized to realize the frequency division absorption of the high and low frequency components in fluctuating power. Simulation and experimental results show that the proposed control strategy can effectively improve the power quality of the system. Compared with the comparison algorithm, the output current THD decreases from 17.09% to 8.23%. At the same time, in the scenario of indoor PPV system, the TVID control strategy is verified.

References

[1] L. Wang, H. Wang, Q. Zhao, H. Yang, H. Zhao, and B. Huang, "Development and prospect of intelligent pavement," *China J. Highway Transport*, vol. 32, no. 4, pp. 50–72, Apr. 2019, doi: 10.19721/j.cnki.1001-7372.2019.04.004.

[2] H. Wang et al., "Research progress and prospect of environment-friendly green road," *J. Central South Univ.*, vol. 52, no. 7, pp. 2137–2169, Jul. 2021, doi: 10.11817/j.issn.1672-7207.2021.07.004.

[3] L. W. Chong, Y. W. Wong, R. K. Rajkumar, R. K. Rajkumar, and D. Isa, "Hybrid energy storage systems and control strategies for stand-alone renewable energy power systems," *Renewable Sustain. Energy Rev.*, vol. 66, pp. 174–189, Dec. 2016, doi: 10.1016/j.rser.2016.07.059.

[4] L. Kouchachvili, W. Yaïci, and E. Entchev, "Hybrid battery/supercapacitor energy storage system for the electric vehicles," *J. Power Sources*, vol. 374, pp. 237–248, Jan. 2018, doi: 10.1016/j.jpowsour.2017.11.040.

[5] S. Kotra and M. K. Mishra, "Design and stability analysis of DC microgrid with hybrid energy storage system," *IEEE Trans. Sustain. Energy*, vol. 10, no. 3, pp. 1603–1612, Jul. 2019, doi: 10.1109/TSTE.2019.2891255.

[6] G. Li, Z. Yang, B. Li, and H. Bi, "Power allocation smoothing strategy for hybrid energy storage system based on Markov decision process," *Appl. Energy*, vol. 241, pp. 152–163, May 2019, doi: 10.1016/j.apenergy.2019.03.001.

[7] X. Li and J. Liu, "Real-time power distribution method adopting second-order filtering for hybrid energy storage system," *Power System Technol.*, vol. 43, no. 5, pp. 1650–1657, May 2019, doi: 10.13335/j.1000-3673.pst.2018.1447.

[8] W. Ma, H. Gao, Y. Zhang, Z. Liu, and F. Peng, "Adaptive PCC power fluctuation smoothing method based on EWT for distributed PV-energy storage," *Power Syst. Protection Control*, vol. 52, no. 3, pp. 51–61, Feb. 2024, doi: 10.19783/j.cnki.pspc.230333.

[9] H. Zheng, L. Xie, L. Ye, P. Lu, and K. Wang, "Hybrid energy storage smoothing output fluctuation strategy considering photovoltaic dual evaluation indicators," *Trans. China Electrotechnical Soc.*, vol. 36, no. 9, pp. 1805–1817, May 2021, doi: 10.19595/j.cnki.1000-6753.tces.201058.

[10] B. Tian, Z. Zhang, and M. Yang, "Research on hybrid energy storage power allocation and capacity determination based on multiple moving average filtering," *Trans. China Electrotechnical Soc.*, vol. 39, no. 5, pp. 1548–1564, Mar. 2024, doi: 10.19595/j.cnki.1000-6753.tces.222348.

[11] B. Hredzak, V. G. Agelidis, and M. Jang, "A model predictive control system for a hybrid battery-ultracapacitor power source," *IEEE Trans. Power Electron.*, vol. 29, no. 3, pp. 1469–1479, Mar. 2014, doi: 10.1109/TPEL.2013.2262003.

[12] F. Garcia-Torres and C. Bordons, "Optimal economical schedule of hydrogen-based microgrids with hybrid storage using model predictive control," *IEEE Trans. Ind. Electron.*, vol. 62, no. 8, pp. 5195–5207, Aug. 2015, doi: 10.1109/TIE.2015.2412524.

[13] J. Ramoul, E. Chemali, L. Dorn-Gomba, and A. Emadi, "A neural network energy management controller applied to a hybrid energy storage system using multi-source inverter," in *Proc. IEEE Energy Convers. Congr. Expo.*, 2018, pp. 2741–2747, doi: 10.1109/ECCE.2018.8558326.

[14] I. J. Cohen, D. A. Wetz, B. J. McRee, Q. Dong, and J. M. Heinzel, "Fuzzy logic control of a hybrid energy storage module for use as a high rate prime power supply," *IEEE Trans. Dielectrics Elect. Insul.*, vol. 24, no. 6, pp. 3887–3893, Dec. 2017, doi: 10.1109/TDEI.2017.006647.

[15] X. Feng, H. B. Gooi, and S. X. Chen, "Hybrid energy storage with multimode fuzzy power allocator for PV systems," *IEEE Trans. Sustain. Energy*, vol. 5, no. 2, pp. 389–397, Apr. 2014, doi: 10.1109/TSTE.2013.2290543.

[16] W. Jiang and B. Fahimi, "Multiport Power Electronic Interface—Concept, modeling, and design," *IEEE Trans. Power Electron.*, vol. 26, no. 7, pp. 1890–1900, Jul. 2011, doi: 10.1109/TPEL.2010.2093583.

[17] Q. Rong et al., "Asymmetric sampling disturbance-based universal impedance measurement method for converters," *IEEE Trans. Power Electron.*, vol. 39, no. 12, pp. 15457–15461, Dec. 2024, doi: 10.1109/TPEL.2024.3451403.

[18] Z. Li, K. W. Chan, J. Hu, and J. M. Guerrero, "Adaptive droop control using adaptive virtual impedance for microgrids with variable PV outputs and load demands," *IEEE Trans. Ind. Electron.*, vol. 68, no. 10, pp. 9030–9640, Oct. 2021, doi: 10.1109/TIE.2020.3022524.

[19] Q. Xu, J. Xiao, P. Wang, X. Pan, and C. Wen, "A decentralized control strategy for autonomous transient power sharing and State-of-charge recovery in hybrid energy storage systems," *IEEE Trans. Sustain. Energy*, vol. 8, no. 4, pp. 1443–1452, Oct. 2017, doi: 10.1109/TSTE.2017.2688391.

[20] Q. Xu et al., "A decentralized dynamic power sharing strategy for hybrid energy storage system in autonomous DC microgrid," *IEEE Trans. Ind. Electron.*, vol. 64, no. 7, pp. 5930–5941, Jul. 2017, doi: 10.1109/TIE.2016.2608880.

[21] Q. Xu, J. Xiao, X. Hu, P. Wang, and M. Y. Lee, "A decentralized power management strategy for hybrid energy storage system with autonomous bus voltage restoration and state-of-charge recovery," *IEEE Trans. Ind. Electron.*, vol. 64, no. 9, pp. 7098–7108, Sep. 2017, doi: 10.1109/TIE.2017.2686303.

[22] P. Lin, P. Wang, J. Xiao, J. Wang, C. Jin, and Y. Tang, "An integral droop for transient power allocation and output impedance shaping of hybrid energy storage system in DC microgrid," *IEEE Trans. Power Electron.*, vol. 33, no. 7, pp. 6262–6277, Jul. 2018, doi: 10.1109/TPEL.2017.2741262.

[23] Y. Zhang and Y. W. Li, "Energy management strategy for supercapacitor in droop-controlled DC microgrid using virtual impedance," *IEEE Trans. Power Electron.*, vol. 32, no. 4, pp. 2704–2716, Apr. 2017, doi: 10.1109/TPEL.2016.2571308.

[24] Z. Wang, P. Wang, W. Jiang, and P. Wang, "A decentralized automatic load power allocation strategy for hybrid energy storage system," *IEEE Trans. Energy Convers.*, vol. 36, no. 3, pp. 2227–2238, Sep. 2021, doi: 10.1109/TEC.2020.3038476.

[25] Y. Gu, W. Li, and X. He, "Frequency-coordinating virtual impedance for autonomous power management of DC microgrid," *IEEE Trans. Power Electron.*, vol. 30, no. 4, pp. 2328–2337, Apr. 2015, doi: 10.1109/TPEL.2014.2325856.

[26] Y. Gu, X. Xiang, W. Li, and X. He, "Mode-adaptive decentralized control for renewable DC microgrid with enhanced reliability and flexibility," *IEEE Trans. Power Electron.*, vol. 29, no. 9, pp. 5072–5080, Sep. 2014, doi: 10.1109/TPEL.2013.2294204.

[27] F. Gao et al., "Comparative stability analysis of droop control approaches in voltage-source-converter-based DC microgrids," *IEEE Trans. Power Electron.*, vol. 32, no. 3, pp. 2395–2415, Mar. 2017, doi: 10.1109/TPEL.2016.2567780.

[28] H. Wang, M. Han, R. Han, J. M. Guerrero, and J. C. Vasquez, "A decentralized current-sharing controller endows fast transient response to parallel DC–DC converters," *IEEE Trans. Power Electron.*, vol. 33, no. 5, pp. 4362–4372, May 2018, doi: 10.1109/TPEL.2017.2714342.

[29] B. She et al., "Inverter PQ control with trajectory tracking capability for microgrids based on physics-informed reinforcement learning," *IEEE Trans. Smart Grid*, vol. 15, no. 1, pp. 99–112, Jan. 2024, doi: 10.1109/TSG.2023.3277330.

[30] B. Stevanović, S. Cóbreces, E. Serban, P. Alou, M. Ordonez, and M. Vasić, "Influence of DC/DC stage on the design of the output filter of the inverter stage in two-stage grid-connected PV systems," in *Proc. IEEE Energy Convers. Congr. Expo.*, 2021, pp. 15–22, doi: 10.1109/ECCE47101.2021.9595248.

[31] M. Uno, D. Cheng, S. Onodera, and Y. Sasama, "Bidirectional buck-boost converter using cascaded energy storage modules based on cell voltage equalizers," *IEEE Trans. Power Electron.*, vol. 38, no. 1, pp. 1249–1261, Jan. 2023, doi: 10.1109/TPEL.2022.3203900.

[32] P. Azer and A. Emadi, "Generalized State space average model for multi-phase interleaved buck, boost and buck-boost DC-DC converters: Transient, steady-state and switching dynamics," *IEEE Access*, vol. 8, pp. 77735–77745, 2020, doi: 10.1109/ACCESS.2020.2987277.

Mingxuan Mao received the Ph.D. degree in control theory and control engineering from Chongqing University, Chongqing, China, in 2017.

From 2016 to 2017, he was a Visiting Scholar with the University of Leeds, Leeds, U.K., where he was engaged in research on renewable energy systems and optimal control of power electronic converters. From 2018 to 2021, he was an Assistant Professor/Lecturer with the School of Electrical Engineering, Chongqing University. From 2021 to 2023, he was an Academic with CAP Group, Department of Electrical and Electronic Engineering, Imperial College London, London, U.K. He is currently a Professor with the School of Automation, Wuxi University, Wuxi, China. His research interests include advanced control theory and application for renewable and energy systems, modeling and control of solar energy power generation, power electronics topologies and intelligence control, and deep learning.

Yuhao Tang received the B.S. degree in automation, in 2024, from the Nanjing University of Information Science and Technology, Nanjing, China where he is currently working toward the M.S. degree in control engineering.

His current research interests include power electronics topologies and control of solar energy power generation.

Fuping Ma received the B.S. degree in electrical engineering and automation from Chongqing University, Chongqing, China, in 2021, and the master's degree in electrical engineering from Chongqing University, Chongqing, China, in 2024.

His current research interests include power electronics topologies and control of solar energy power generation.

Haojin Sun is currently working toward the B.S. degree in electrical engineering and automation from Wuxi University, Wuxi, China.

His current research interests include power electronics topologies and control of solar energy power generation.

Guoxiang Hua was born in Jiangsu Province, China, in 1985. He received the B.S. and M.S. degrees in electrical engineering, in 2008 and 2011, respectively, from North China Electric Power University, Beijing, China, where he is currently working toward the Ph.D. degree in electrical engineering.

Since his appointment as an Associate Professor and Master's Supervisor, he has been with the School of Automation, Wuxi University, Wuxi, China. His research interests include smart grids, machine learning, power communication, and intelligent control.

Peng Li received the B.S. degree in electronic engineering from the Nanjing University of Science and Technology, Nanjing, China, in 1990, the M.S. degree in electronic science and technology from the China University of Mining and Technology, Xuzhou, China, in 2003, and the Ph.D. degree in biomedical engineering from Xi'an Jiaotong University, Xi'an, China, in 2008.

He is currently a Professor with the School of Automation, Wuxi University, Wuxi, China, and the School of Automation, Nanjing University of Information Science and Technology, Nanjing, China. His current research interests include detection technology and automatic equipment, power electronics topologies, meteorological sensors and instruments, and ultrasonic imaging and related signal processing.